Local synaptic inputs support opposing, network-specific odor representations in a widely projecting modulatory neuron

Xiaonan Zhang[1], Kaylynn Coates[2], Andrew Dacks[2], Cengiz Gunay[3], J. Scott Lauritzen[4], Feng Li[4], Steven A. Calle-Schuler[4], Davi Bock[4,5], Quentin Gaudry[1+]

[1] Department of Biology, University of Maryland, College Park, MD 20742, USA

[2] Department of Biology, West Virginia University, Morgantown, WV 26506, USA

[3] School of Science and Technology, Georgia Gwinnett College, Lawrenceville, GA 30043, USA.

[4] Janelia Farm Research Campus, Howard Hughes Medical Institute, Ashburn, VA 20147, USA

[5] Department of Neurological Sciences, Larner College of Medicine, University of Vermont, 89 Beaumont Avenue, Burlington, VT 05405

[+]Corresponding author
Quentin Gaudry
1108 Biosciences Research Building B1-58
University of Maryland, College Park
College Park, MD 20742
qgaudry@umd.edu
(301) 405-9451

Significance

The centrifugal innervation of neuronal circuits is ubiquitous across centralized nervous systems. Such inputs often arise from modulatory neurons that arborize broadly throughout the brain. How information is integrated in such cells and how release from their distant terminals is regulated remains largely unknown. We show that a serotonergic neuron that innervates multiple olfactory networks in *Drosophila* has opposite polarity odor responses in the antennal lobe and lateral horn, the first and second order olfactory neuropils respectively. The neuron's processes in the antennal lobe are inhibited by odors which shunts odor specific activity in the lateral horn. Our results show that serotoninergic modulation in flies occurs predominantly in higher order olfactory structures through a combination of both local synaptic integration and dendrite wide computations.

Abstract

Serotonin plays different roles across networks within the same sensory modality. Previously, we used whole-cell electrophysiology in *Drosophila* to show that serotonergic neurons innervating the first olfactory relay are inhibited by odorants (Zhang and Gaudry, 2016). Here we show that network-spanning serotonergic neurons segregate information about stimulus features, odor intensity and identity, by using opposing coding schemes in different olfactory neuropil. A pair of serotonergic neurons (the CSDns) innervate the antennal lobe and lateral horn, which are first and second order neuropils. CSDn processes in the antennal lobe are inhibited by odors in an identity independent manner. In the lateral horn, CSDn processes are excited in an odor identity dependent manner. Using functional imaging, modeling, and EM reconstruction, we demonstrate that antennal lobe derived inhibition arises from local GABAergic inputs and acts as a means of gain control on branch specific inputs that the CSDns receive within the lateral horn.

Keywords: neuromodulation, *Drosophila*, olfaction, serotonin, multicompartmental model, sensory

Introduction

Virtually all neuronal circuits are subject to neuromodulation from both neurons intrinsic to a network and extrinsic centrifugal sources (Katz, 1995; Lizbinski and Dacks, 2017). In vertebrates, extrinsic modulation is often supplied by nuclei located deep within the brainstem that release a variety of transmitters such as norepinephrine (NE) (Schwarz and Luo, 2015), serotonin (5-HT) (Charnay and Léger, 2010; Hornung, 2003), dopamine (DA) (Ikemoto, 2007; Lammel et al., 2008), or acetylcholine (Ach) (Wenk, 1997). For example, the olfactory bulb (OB) in mammals receives a tremendous amount of centrifugal innervation (Padmanabhan et al., 2019) that can be critical for proper olfactory behavior (Nunez-Parra et al., 2013). However, by spanning and innervating most cortical and subcortical regions, modulatory systems target multiple points along the sensory-motor axis of functional circuits. A prominent view of such modulatory systems is that they provide a mechanism for top-down regulation of sensory processing (Jacob and Nienborg, 2018; Thiele and Bellgrove, 2018) and help coordinate activity across brain regions (Melzer et al., 2012). Modulatory systems are traditionally regarded as integrate-and-fire models where the neurons integrate synaptic inputs in their dendrites within their local nuclei and use action potentials to broadcast this signal to release sites across sensory networks. Such models imply that modulator release will be inherently correlated across distal targets. However, as virtually all axons are subject to pre-synaptic regulation (Miller, 1998), it is likely that most centrifugal modulatory neurons are subject to local influences by the circuits that they infiltrate. This suggests that the local release of transmitters from such systems may instead be decorrelated across brain regions. Decorrelating transmitter release across brain regions is advantageous, as it would provide greater flexibility in how neuromodulation may be employed. How transmitter release is locally regulated in modulatory neurons and how signals propagate through their processes has been exceedingly difficult to study in vertebrate systems due to many contributing factors. First, the vertebrate cerebrum is large and imaging the extensive processes of such neurons across brain areas requires specialized tools (Lecoq et al., 2014; Sofroniew et al., 2016; Stirman et al., 2016; Terada et al., 2018). Second, individual modulatory neurons within the same brainstem nucleus are highly heterogeneous in their projection patterns (Gagnon and Parent, 2014; van der Kooy and Kuypers, 1979) making it difficult to assign activity across brain regions to individual cells. Additionally, the spatial pattern of extrinsic input activation can also be stimulus specific. For example, different odors can activate unique presynaptic terminals from piriform neurons that feed back into the OB (Otazu et al., 2015). But whether such odor responses in centrifugal inputs arise from the recruitment of different individual cortical neurons or from local axo-axonic

interactions within the OB remains unknown. The spatial pattern of cholinergic input to the OB is also odor-specific and arises through similarly undescribed mechanisms (Rothermel et al., 2014).

The *Drosophila* brain is an ideal preparation to study how signals propagate through wide-field modulatory neurons because such cells are often stereotyped and can be genetically targeted across individual flies. For example, only one serotonergic neuron per hemisphere, termed the contralaterally-projecting serotonin-immunoreactive deuterocerebral neuron (CSDn), innervates both the first and second order olfactory neuropils in the fly brain (Coates et al., 2017; Dacks et al., 2006; Roy et al., 2007; Sun et al., 1993) (*Figure 1A*). CSDns can be targeted genetically (Roy et al., 2007) and affect various olfactory behaviors involving appetitive (Xu et al., 2016) and pheromonal odorants, including cis-vaccenyl acetate (cVA) (Singh et al., 2013). The modulation of cVA-evoked behavioral responses is especially interesting because the CSDns are thought to participate in top-down modulation and to have their effects mainly in the first olfactory relay, the antennal lobe (AL) (Hill et al., 2002; Singh et al., 2013; Sun et al., 1993). However, CSDn processes avoid the cVA-sensitive DA1 glomerulus (Coates et al., 2017; Zhang and Gaudry, 2016) and DA1 projection neuron (PN) odor responses are not modulated with strong CSDn stimulation (Zhang and Gaudry, 2016). Finally, whole-cell recordings show strong inhibition of the CSDn during stimulation with cVA (Zhang and Gaudry, 2016). This suggests that the modulatory effects of the CSDns on cVA-guided behavior may not occur in the AL, but rather in one of the other olfactory neuropil that the CSDns innervate. Because the CSDns express pre- and postsynaptic markers throughout their arborizations (Zhang and Gaudry, 2016), it is possible that transmitter release is locally regulated via inputs from their target networks (Gaudry, 2018) and that olfactory-mediated modulation occurs predominantly downstream of the AL. In this study we employed 2-photon calcium imaging, electron microscopy, and compartmental modeling to show that the CSDns integrate synaptic inputs locally within their target regions giving rise to distinct odor evoked activity patterns within different olfactory neuropil.

Results

To examine how CSDns contribute to olfactory processing across brain regions, we employed GCaMP6s (Chen et al., 2013) and 2-photon volumetric microscopy to characterize olfactory responses across their arbors. We initially imaged CSDn neurites in the AL (*Figure 1B*, *Figure 1-video 1*) and found that nearly all compounds in a diverse panel of odorants resulted in

inhibition (*Figure 1C*, *1D* and *Figure 1 - figure supplement 1*). The only exception was ammonia, which produced a weak level of excitation as previously reported in whole-cell somatic recordings (Zhang and Gaudry, 2016). These results are consistent with previous studies demonstrating that odors generally inhibit the CSDns during electrophysiological somatic recordings (*Figure 1E*) (Zhang and Gaudry, 2016), which is due to prominent input from GABAergic local interneurons (LN) (Coates et al., 2017; Zhang and Gaudry, 2016).

Inhibition in the AL scales with increasing odor intensity and the spatial pattern of activation of GABAergic LNs is odor invariant (Hong and Wilson, 2015). Inhibition of the CSDn also scales with odor intensity (Zhang and Gaudry, 2016), but it is unknown if unique odors can recruit distinct spatial patterns of CSDn activity within its dendrites in the AL. We used principal components analysis (PCA) to examine the spatial profile of CSDn inhibition in response to our odor panel. This analysis revealed that only the first PC generated a structured image showing inhibition in the AL while PC2 captured the excitation resulting from stimulation with ammonia (*Figure 1F*). Thus, aside from ammonia, CSDn processes in the AL receive odor-invariant inhibition, and this inhibition scales with odor intensity (Zhang and Gaudry, 2016).

We next examined CSDn processes in the lateral horn (LH; *Figure 2A*), a brain region that receives direct input from the AL and mediates innate olfactory behaviors (de Belle and Heisenberg, 1994). Surprisingly, we found that every odorant in our panel produced excitation in the CSDn LH arbors (*Figure 2B, Figure 2-video 1*). Furthermore, PCA revealed that CSDn odor responses in the LH varied spatially (*Figure 2C, Figure 2 - figure supplement 1*) and displayed a greater coefficient of variation compared to responses in the AL (*Figure 2D*). These results show that the processes of the CSDn have opposing responses to odor stimulation across different olfactory regions (*Figure 2E*). The CSDn has both pre- and postsynaptic sites in the LH (Zhang and Gaudry, 2016), so GCaMP signaling could represent either the activation of CSDn postsynaptic receptors or calcium influx at presynaptic release sites. Some GCaMP signaling in the LH must represent local activation of postsynaptic receptors in the CSDn since its AL processes are simultaneously inhibited. To assess whether this activity also correlates with synaptic release from the CSDn, we employed sytGCaMP6s, a variant of the calcium sensor that is tethered to synaptotagmin and trafficked to presynaptic release sites (Cohn et al., 2015). Olfactory stimulation showed increased sytGCaMP6s signaling (*Figure 2 - figure supplement 2*), suggesting odorants likely evoke transmitter release in the LH processes of the CSDn.

To determine if spatial patterns of CSDn odor-evoked activity in the LH were odor-specific, we quantified the similarity between CSDn odor responses by first computing the spatial correlation between them (*Figure 3A*). We then calculated the Euclidean linkage distance

between all odor correlations to illustrate which odors are most similarly encoded in the neurites of the CSDn in the LH (*Figure 3B*). How might odor specific responses arise in the CSDn processes in the LH? PNs are a potential source of excitatory input to the CSDns in the LH as they are cholinergic, and their axons segregate anatomically (Jefferis et al., 2007; Tanaka et al., 2004) and functionally (Min et al., 2013; Seki et al., 2017; Strutz et al., 2014) in this region. We compared the odor representations of PN and CSDn processes within this structure to determine if PNs may provide excitatory drive to the CSDn branches in the LH. The linkage distance between the spatial pattern of odor responses was highly correlated between PN and CSDn responses in the LH (*Figure 3C* and *Figure 3 – figure supplement 1*). These data suggest that PNs may provide direct synaptic input onto the CSDn locally in the LH. Using synaptobrevin GFP Reconstitution Across Synaptic Partners (syb:GRASP) (Feinberg et al., 2008; Macpherson et al., 2015) we observed a positive signal for PNs synapsing onto the CSDns (*Figures 3D-F*) in the LH. We further verified this synaptic connection by looking at the connectivity of a CSDn reconstructed within a whole fly brain EM dataset (Zheng et al., 2018). PNs from at least 17 glomeruli (presynaptic PN tracings provided as a personal communication from Greg Jefferis, Phillipp Schlegel, Alex Bates, Marta Costa, Fiona Love and Ruari Roberts) show direct input to the CSDn throughout the LH (*Figures 3G-I*). Together these results suggest that the CSDns receive input from different cell classes in the AL and LH to shape its olfactory responses locally. In the AL, GABAergic LNs constitute a major input to the CSDns and drive inhibitory responses independent of odor identify. PNs make relatively few synaptic connections with the CSDns in the AL (Coates et al., 2017). In the LH, olfactory responses in the CSDn neurites are excitatory, odor specific, and are likely in part shaped by direct PN input.

The function of a neuron is often dictated by the manner in which synaptic inputs are integrated across its dendritic arbor. We therefore asked whether the AL and LH neurites of the CSDn function as electrotonically independent compartments within the same cell, or if signals propagate between regions during odor sampling. To examine how voltage spreads throughout the CSDn, we built a passive compartmental model based on an anatomical reconstruction of the CSDn generated from the whole fly brain EM dataset (Carnevale and Hines, 2006; Zheng et al., 2018) (*Figures 4A* and *Figure 4 – figure supplement 1*). While such models ignore the contributions of active conductances or variations in passive properties across dendrites, they can nevertheless provide insight into signal propagation and help formulate hypotheses. The model was generated by adjusting the membrane capacitance (C_m), the membrane conductance (g_{leak}), and the axial resistance (R_a) so that simulated current injections into the model soma matched physiological responses taken *in vivo* (*Figures 4B*). A wide range of

models with varying properties provided reasonable fits to the *in vivo* CSDn recordings. In these models, injecting simulated hyperpolarizing IPSPs into the AL resulted in varying amounts of spread throughout the neurites of the CSDn. In some models, the hyperpolarization was constrained only to the local injection site (*Figure 4C*), while in other models the hyperpolarization spread throughout the AL (*Figure 4D*). However, whole-cell recordings *in vivo* show that the inhibition arising from the AL indeed spreads to the soma (Zhang and Gaudry, 2016). Several of the models that we generated displayed this property. Importantly, all models that displayed somatic inhibition when current was injected into the CSDn processes in the AL also showed inhibition in the LH (*Figure 4E*). These results suggest that the geometry and passive properties of the CSDn allow the propagation of inhibition from the AL to the LH during olfactory stimulation.

The propagation of voltages through the dendrites of neurons is not always symmetrical and can be biased by impedance mismatches as well as differences in the diameters of intersecting branches (Stuart et al., 2016). We therefore asked if voltage changes generated in the LH would propagate as efficiently to the AL compared to the opposite direction. We injected current into the either the LH or the AL of the model to elicit voltage changes of similar magnitudes and calculated the proportion of the signal that propagated to the other region. This approach revealed that the geometry of the CSDn arbors favor the propagation of voltage signals from the AL preferentially to the LH (*Figure 4F*).

If voltage signals preferentially propagate from the AL to the LH, one would predict that isolating the CSDn processes in the LH from the rest of the CSDn would boost any odor evoked excitation due to local input within the LH. We therefore used 2-photon laser ablation to sever the CSDn neurites just proximal to their entrance into the LH. This manipulation isolates the LH processes of the CSDn from the AL, while still allowing these neurites to respond to synaptic input within the LH (*Figure 4G and H*). Olfactory responses to all odors tested increased in the processes of the CSDn in the LH following the removal of AL inhibition (*Figure 4I, J,* and *K*). As a control for the non-specific damage of laser ablation, we severed the branches of the CSDn in the contralateral hemisphere and found that this had no impact on odor responses in the intact branches of the CSDn in the ipsilateral LH (*Figure 4K*). These results demonstrate that during normal odor sampling, inhibition from the AL propagates to suppress olfactory responses in the LH.

Discussion

There has been a recent interest in characterizing the structures that provide input to serotonergic neurons in vertebrates in an attempt to understand the types of processes that might impact 5-HT release (Sparta and Stuber, 2014). Such studies relied on genetically restricted retrograde labeling to identify regions that provide monosynaptic inputs to serotonergic raphe neurons (Ogawa et al., 2014; Pollak Dorocic et al., 2014; Weissbourd et al., 2014). Our functional approach of calcium imaging across brain regions is complementary but has the advantage of revealing where signals are integrated and determining whether the net effect of that integration within is excitatory or inhibitory. Here we show that a serotonergic neuron with broad arbors integrates locally at multiple neuropil along to the olfactory pathway in *Drosophila*. Interestingly, synaptic inputs at the first and second order processing stages of olfaction impose opposite polarity responses in this neuron and likely decorrelate synaptic release in distinct target regions. Inhibition dominates responses in the AL and odor-specific excitation is prominent in the downstream LH. This suggests that across a single widely projecting modulatory neuron, branches within distinct neuropils can operate in different manners.

Local regulation of release in modulatory neurons

Classical methods of studying the activation of modulatory systems during sensory processing in vertebrates rely heavily on recording extracellular spikes in the nuclei that house the neurons' somas. However, invertebrate studies involving motor systems have shown compartmentalization of neurons spanning distant neuropils (Nikitin et al., 2013; Sasaki et al., 2007). Our results demonstrate that the activity within a single serotonergic neuron can vary across neuropils involved in processing the same sensory modality. As a given modulator may perform distinct functions in different brain regions, local regulation of release allows these functions to be employed independently. For instance, 5-HT in the OB indirectly inhibits OSN terminals and has been proposed to serve a gain control function (Petzold et al., 2009), while in the piriform cortex 5-HT has no effect on stimulus input, but rather only decreases spontaneous activity (Lottem et al., 2016). Additionally, 5-HT has different effects on mitral cells in the main versus mitral cells in the accessory olfactory bulb (Huang et al., 2017). Local regulation of 5-HT release would allow these processes to be engaged in an independent and combinatorial manner, and thus allow for a greater net overall modulatory capacity.

Local regulation and decoupling of modulator release across synaptic sites is not unique to invertebrates and has been implicated in the normal function of the mammalian DA system. First, DA release is only partially correlated with firing activity, and release can be locally evoked

in the absence of spiking in DA cells (Floresco et al., 1998). Additionally, local inactivation of the nucleus accumbens (NA) decreases DA release in the NA without impacting DA neuron firing (J. L. Jones et al., 2010). This has led to the theory that DA release can signal both motivation and reward prediction errors (RPE) on similar timescales (Hamid et al., 2015). Dopamine release related to motivation is thought to be shaped by local presynaptic mechanisms while dopamine related to RPE correlates more strongly with the firing properties of DA neurons (Berke, 2018). Measuring serotonergic transmission across release sites is more difficult compared to dopamine (Dankoski and Wightman, 2013), nevertheless, it is highly likely that 5-HT is also regulated by local presynaptic mechanisms (Egashira et al., 2002; Schlicker et al., 1984; Tao and Auerbach, 1995; Threlfell et al., 2004). Whether there is local regulation of 5-HT release in the vertebrate olfactory system is more controversial. EM reconstructions of raphe terminals in the OB have failed to reveal postsynaptic densities in raphe axons (Gracia-Llanes et al., 2010; Suzuki et al., 2014). This may be because such input is extra synaptic (Gaudry, 2018), as is the case with $GABA_B$ receptors in the raphe nucleus proper (Varga et al., 2002).

Multi-dendritic processing

Local integration in the AL and LH allow the CSDn to independently process and shape sensory information at multiple points in the early olfactory pathway of the fly. Specifically, we found that PN axons directly excite CSDn terminals in the LH in an odor specific manner while CSDn branches in the AL are inhibited. Previous studies have shown that the CSDn soma is also inhibited by odors and that stimulation of the CSDn has little impact on olfactory circuitry in the AL (Zhang and Gaudry, 2016), despite the CSDn being critical for normal olfactory behavior (Singh et al., 2013; Xu et al., 2016). Our current study resolves this issue by suggesting instead that the CSDn modulates behavior by affecting odor-processing in the LH (*Figures 4* and *Figure 4 – figure supplement 2*), which has previously been unexplored. What then is the purpose of odor-evoked inhibition in the AL? Inhibition of CSDn processes in the AL does not appear to depend on odor identity as shown in this study, but rather correlates with the total amount of ORN activity that an odor elicits (Zhang and Gaudry, 2016). This can vary with both odor identity or concentration. Our compartmental modeling shows that AL and LH processes of the CSDn are electrotonically connected, but that voltage preferentially passes from the AL to the LH. As CSDn inhibition scales with increasing odor strength due to robust GABAergic LN input in the AL (Coates et al., 2017; Zhang and Gaudry, 2016), this inhibition shunts LH responses proportionally. This configuration ultimately allows olfactory modulation to be odor specific in the LH while being less dependent on odor concentration. Multi-dendritic computing is critical for

processing other sensory modalities as well (Ranganathan et al., 2018), but most notably vision (P. W. Jones and Gabbiani, 2010; Koren et al., 2017). Synaptic integration between dendrites is used to compute object motion across the visual field on a collision course with the observer. Interestingly, the dendrites of starburst amacrine cells in the mammalian retina express mGluR to isolate dendritic compartments thus preventing integration to non-preferred stimuli while enabling regulated integration specifically to preferred directions of motion (Koren et al., 2017). Our laser ablation experiments demonstrate that CSDn neurites influence one another during olfaction, but it is intriguing that the magnitude of such coupling could be state dependent and regulated by active conductances.

Top-down versus bottom-up neuromodulation

The CSDn was originally proposed to participate in top-down modulation by transmitting higher order sensory information from the LH to the AL (Hill et al., 2002; Sun et al., 1993). However, direct evidence for top-down modulation via the CSDn has never been demonstrated. Our results suggest that during olfaction, the CSDn acts more in a bottom-up fashion where responses in the AL have a greater impact on downstream processing in the LH. Transmitter release during olfactory sampling putatively occurs only later in the sensory processing stream rather than at the earliest stages. Interestingly, the CSDn has numerous release sites in the AL (Coates et al., 2017; Sun et al., 1993; Zhang and Gaudry, 2016) and CSDn derived 5-HT directly inhibits several classes of neurons in the AL (Zhang and Gaudry, 2016). But how are CSDn release sites activated in the AL? Olfaction clearly inhibits both the processes of the CSDn in the AL as well at its spike initiation site (Zhang and Gaudry, 2016). However, it is likely that the CSDn also receives input from unidentified non-olfactory sources that excite the neuron's spike initiation site allowing it to modulate in a top-down manner. Further reconstruction of the CSDns inputs in the EM data set will reveal candidates for further physiological evaluation. Thus, non-olfactory stimulation of the CSDn may be consistent with top-down modulation and would constitute one mechanism by which a broadly arborizing modulatory neuron may be multifunctional depending on the source of its excitatory drive. Multifunctional neurons have been well described in central pattern generating networks (Briggman and Kristan, 2008) but are only recently becoming appreciated with regards to neuromodulation (Berke, 2018). Local synaptic interactions within the AL could shape 5-HT release as well to alter olfactory coding in a glomerulus specific fashion (Kloppenburg and Mercer, 2008). Our findings in *Drosophila* suggest that integration into local circuits allows modulatory cells greater flexibility in how they participate in sensory processing and may be a

feature that is often overlooked when assessing the function of these critical components of the central nervous system.

Methods

Odors and odor delivery

Odors were presented as previously described (Zhang and Gaudry, 2016). In brief, a carrier stream of carbon-filtered house air was presented at 2.2L/min to the fly continuously. A solenoid was used to redirect 200 ml/min of this air stream into an odor vial before rejoining the carrier stream, thus diluting the odor a further 10-fold prior to reaching the animal. All odors were diluted 1:100 in paraffin oil (J.T. Baker VWR #JTS894), except for acids, which were diluted in distilled water. All odors were obtained from Sigma Aldrich (Saint Louis, MO) except for cVA, which was obtained from Pherobank (Wageningen, Netherlands). cVA was delivered as a pure odorant. In our olfactometer design, the odor vial path was split to 16 channels each with a different odor or solvent control. Pinch valves (Clark Solutions, Hudson MA part number PS1615W24V) were used to select stimuli between each trial. Each odor was presented sequentially one trial at a time. Each odor was presented 3-4 times within a preparation and the mean of these responses were then averaged across animals.

Odors	**Supplier**
Paraffin oil	J.T.Baker CAS: 8012-95-1
Ammonium hydroxide	Sigma-Aldrich CAS: 1336-21-6
Ethyl acetate	Sigma-Aldrich CAS: 141-78-6
Methyl salicylate	Sigma-Aldrich CAS: 119-36-8
Benzaldehyde	Sigma-Aldrich CAS: 100-52-7
3-hexanone	Sigma-Aldrich CAS: 589-38-8
p-cresol	Sigma-Aldrich CAS: 106-44-5

1-octen-3-ol	Sigma-Aldrich CAS: 3391-86-4
Geranyl acetate	Sigma-Aldrich CAS: 105-87-3
cVA	Pherobank, Wijk bij Duurstede, Netherlands
geosmin	Sigma-Aldrich CAS: 16423-19-1
acetic acid	Sigma-Aldrich CAS: 64-19-7

346

347 **Fly Genotypes**

348 The following *Drosophila* genotypes were used in this study: w; UAS-GCaMP6s; R60F02-Gal4,
349 UAS-GCaMP6s, w; NP2242-Gal4/Cyo; R60F02-Gal4, UAS-GCaMP6s, w; GH146-Gal4/+; UAS-
350 GCaMP6s/+ and w; UAS-CD4:spGFP11/Q-GH146; QUAS-syb:spCFP1-10/R60F02-Gal4. PN
351 odor responses were measured in flies expressing the GH146-Gal4 and UAS-GCaMP6s
352 transgenes. To produce the singleton CSDn in Figure 1A, we used UAS-myrGFP, QUAS-
353 mtdTomato-3xHA/+; trans-Tango/+; Gal4-MB465C/+ which occasionally labeled individual
354 CSDns. Flies were generated from the following stocks.

355

Genotype	**Source**	**RRID**
20XUAS-IVS-GCaMP6s (attP40)	BDSC	BDSC_42746
GMR60F02-GAL4 (attP2)	BDSC	BDSC_48228
20XUAS-IVS-GCaMP6s (VK00005)	BDSC	BDSC_42749
GH146-Gal4	BDSC	BDSC_30026
UAS-CD4:spGFP11	BDSC	BDSC_64315
GH146-QF2	BDSC	BDSC_66480
QUAS-syb:spCFP1-10	Marco Gallio, Northwestern University	
UAS-myrGFP, QUAS-mtdTomato-3xHA; trans-Tango	BDSC	BDSC_77124
MB465C-Gal4	BDSC	BDSC_68371
NP2242-Gal4	DGRC	104134

356 BDSC, Bloomington Drosophila Stock Center, Bloomington Indiana. DGRC, Kyoto Stock Center,
357 Kyoto Japan.

Calcium imaging of odor-evoked activity

Female flies aged 3-5 weeks post-eclosion and reared at room temperature were used. In vivo imaging experiments were performed at room temperature. The brain was constantly perfused with saline containing (in mM): 103 NaCl, 3 KCl, 5 N-tris(hydroxymethyl)methyl-2- aminoethane-sulfonic acid, 8 trehalose, 10 glucose, 26 $NaHCO_3$, 1 NaH_2PO_4, 2 $CaCl_2$, and 4 $MgCl_2$ (adjusted to 270–275 mOsm). The saline was bubbled with 95% O_2/5% CO_2 and reached a pH of 7.3. 920 nm wavelength light was used to excite GCaMP6s under two-photon microscopy. The microscope and data acquisition were controlled by ThorImage 3.0 (Thorlabs, Inc.). Three-dimensional volumes of neuropil were used to measure odor responses. Volumes consisted of 6 – 8 frames separated by 5 - 6 μm in the z plane between frames. The volumes were scanned at 60 frames / second and thus a 6 – 7 complete volumes were imaged each second. Single imaging trials consisted of 90 volumes at a resolution of 256×256 pixels. Odors were delivered for 1 second after the first 2 seconds of each trial. An 80 second interval between each trial was applied to allow replenishing of the odor vial head space and to prevent photobleaching of GCaMP. Odors were presented sequentially such that each odor was presented every 16 minutes.

To quantify odor responses, we first generated the mean z-projection for every volume within a trial. Calcium transients (ΔF/F) were then measured as changes in fluorescence, in which ΔF/F was calculated by normalizing the fluorescence brightness changes over the baseline period (the first 2 seconds of each trial before the odor delivery). To reduce noise, a Gaussian low-pass filter of 4×4 pixels in size was then applied to raw ΔF/F signals prior to further analysis.Some trials contained motion artifacts that were removed using StackReg plugin for ImageJ. This motion correction was done on an individual trial basis. The frame containing the peak response was identified by plotting the ΔF/F in an ROI as a function of frame number. The peak calcium signal for each trial was computed as the average of three consecutive frames centered on the frame of the peak response. We set the peak window the same for all trials within a preparation. For each odor stimulus, data was pooled by averaging the peak odor-evoked calcium signal across 3-4 repeats. All imaging data is available at https://drive.google.com/drive/folders/1KVh6aIQ6S_MWyuY7JOwXZ0efgrReFTPv?usp=sharing

Statistical analysis of calcium imaging

Principal Component Analysis (PCA) was applied on the spatial pattern of the peak calcium signal (ΔF/F) in each trial (the mean frame of 2 -3 volumes during the peak odor response).

PCA was computed using the “princomp” function in Matlab (Mathworks, Natick, MA). First an odor response was generated for each trial as described above as the mean response of 2 – 3 volumes during the peak response and averaged across 3 – 4 odor presentations per fly. The resulting image for each odor was converted into a 1-dimensional array consisting of 65,536 elements generated from the original 256 by 256 image). The odor response arrays were inserted as columns for the PCA input matrix. This matrix thus consisted of 12 columns, each representing an odor response. The output PCs were later reshaped back to 256 by 256 matrices for display purposes. The coefficient of variation was also calculated on the same vectorized odor response matrix so that a CV was generated for each pixel across odor responses and then averaged within that preparation. Thus, our reported CV incorporates variance for both the spatial profile and amplitude components of the responses. Correlations between odor responses within the LH were also performed using the same mean responses that served as inputs to the PCA. To calculate the diversity of response patterns to different odors we applied Linkage Hierarchical Clustering. The Euclidean distances between correlation pairs was calculated used as a parameter for clustering. Distances were normalized to the maximum distance within each preparation and then averaged across flies. A regression analysis was applied to compare the similarity between the odor response patterns of the CSDn and PNs in the LH. Our data set consisted of 12 odorants and thus 66 Euclidian distances were calculated for the regression. The p-value and the square of correlation coefficient (R^2) were calculated as the indicator of similarity for each odor response pattern pairs evoked. Two-tailed paired t-tests were performed for all comparisons between before laser ablation and after laser ablation within the same group. All statistical functions were applied in Matlab.

CSDn EM Reconstruction:

The CSDn was identified and partially reconstructed in the female adult fly brain (FAFB) dataset as described in Zheng et al 2018 using CATMAID (Saalfeld et al., 2009; Schneider-Mizell et al., 2016, available at https://catmaid-fafb.virtualflybrain.org). The CSDn reconstruction from the cell body along the primary and secondary arbors leading into the LH as well as tertiary and quaternary branches into the lateral horn were reviewed by a second observer back to the primary branch as previously described (Zheng et al., 2018). For the multi-compartmental model, measurements of the CSDn branch radius (to inform axial resistance parameters) were taken at 7 locations along the primary arbor between the contralateral AL and protocerebrum, 5 locations along the second order branch leading into the lateral horn and 6 locations along primary and secondary branches within the lateral horn. For each location, 20-50 measures of

axon radius were taken from consecutive tissue sections. Data on the projection neurons that are pre-synaptic to CSDn in the FAFB dataset were provided as a personal communication from Greg Jefferis, Phillip Schlegel, Alex Bates, Marta Costa, Fiona Love and Ruari Roberts.

Model construction

A multi-compartmental conductance-based computer model of the CSDn neuron was constructed by taking its electron micrograph reconstruction and importing it into the Neuron simulator (Carnevale and Hines, 2006). An initial reconstruction contained more than 60,000 nodes, but a simplified version of it was generated with 6,056 compartments in the Neuron simulator that retained its basic anatomical and electrotonic structure. The passive cable parameters (axial resistance R_a, leak conductance g_{pas}, leak reversal E_{pas}, and specific capacitance C_m) were fitted using Neuron's RunFitter algorithm. For fitting, we used recorded responses to stimuli of current-clamp and voltage-clamp steps and current-clamp white noise generated by Matlab (Mathworks, Natick, MA). Whole-cell recordings of the CSDn were performed as previously described (Zhang and Gaudry, 2016). The series resistance for CSDn recordings was approximately 10MΩ, and input resistance was 500 - 600MΩ. The pipette resistance was between 8 - 10MΩ. The reversal potential of the CSDn was -45mV. While fitting, parameters were restricted by physiological ranges (R_a between 0.0001-5000 Ωcm, C_m between 0.1-2 μF/cm^2, g_{leak} between 10^{-6}-0.1 S/cm^2, and Epas had unlimited range in mV, *Supplementary File 1*). For a given model, each compartment had the same values for Ra, gpas, Epas, and Cm. Only the difference in process thickness changed the passive properties of the compartments. The resulting passive model of the CSDn neuron was simulated using Neuron's default integration method with a time step of 0.025 ms.

Table 1: Morphological statistics of CSDn neuron sections used in Figure 4E and F.

	L [μm]	Diam [μm]	Area [μm^2]	R_i [MΩ]	C_m [pF]	g_{pas} [nS]
Whole cell	11031.21	0.05	1611.09	370.28	16.11	4.26
Cell body	308.15	0.27	258.89	0.31	2.59	0.68
LH	3758.09	0.04	474.12	169.05	4.74	1.25
AL	6245.41	0.04	787.66	281.13	7.88	2.08

L, total length of section branches; Diam., length-weighted equivalent diameter of section; Area, surface area, R_i, resistance of from beginning to middle of section; C_m, total maximal capacitance of section (does not consider decay of voltage); g_{pas}, total area-scaled leak conductance of the equivalent section.

To investigate how the passive signal travels from the AL to the other parts of the CSDn, we randomly picked ten spots within the AL and injected a square wave of current into the model to elicit a maximum voltage response ranging from about 2 mV to 20 mV. This was repeated 6 times in each condition. We monitored the voltage changes in the windows shown in Figure 4. The windows we set were for the cell body, the center of AL (three randomly selected monitor sites) and the LH (three randomly selected monitoring sites). The average voltage changes of each window were shown in the Figure 4. To investigate how signals preferentially propagated along the CSDn, the same method was applied to LH, so that current was injected in the LH and voltage change windows of interests across the CSDn were kept the same. The process was then repeated with current injection into the AL. The CSDn dendritic architecture does not represent a unique solution to asymmetrical voltage propagation. We were able to reproduce a similar phenomenon using a simpler 3 compartment model consisting of only a soma, an AL branch and a LH branch. The only requirement is to have differences in the resistances of two adjoining dendrites as predicted by cable theory (Rall and Agmon-Snir 1998).

Laser Transection

The transection window was guided by the Gcamp6s basal fluorescence at 920 nm, at about 20 μm before the CSDn neurites enter the lateral horn. An 80mW laser pulse, which consisted of 10 repetitions of continuous frame scanning with 8 μsec of pixel dwell time, at 800 nm was then applied onto this window. A total estimated energy of 0.05 J was thus applied. Successful transection usually resulted in a small cavitation bubble (shown in Figure 4).

KCl induction of GRASP and Immunohistochemistry

In brief, brains used for the induction of syb:GRASP were dissected and rinsed three times with a KCl solution (Macpherson et al., 2015). The brains were then fixed in 4% paraformaldehyde for 20 min. We used the following primary and secondary antibodies at the indicated dilutions: 1:1000 rabbit anti-5HT Sigma (S5545), 1:50 chicken anti-GFP Invitrogen (A10262), 1:100 mouse anti-GFP (referred as anti-GRASP, Sigma #G6539, ref:3), 1:500 rat anti-N-Cadherin (Developmental Studies Hybridoma Bank, DN-Ex #8), 1:250 Alexa Fluor 633 goat anti-rabbit (Invitrogen, A21071), 1:250 Alexa Fluor 488 goat anti-chicken (Life Technologies, A11039),

1:250 Alexa Fluor 568 goat anti-mouse lgG (Life Technologies, A11004) and 1:1000 Alexa Fluor 647 donkey anti-rat IgG (AbCam, ab150155). Brains were mounted and imaged in Vectashield mounting medium (Vector Labs). All steps were performed at room temperature. Confocal z-stacks for the syb:GRASP experiments were collected with a Zeiss LSM710 microscope using a 63× oil-immersion lens and the z-stack of GFP expression in Figure 1A was collected with an Olympus FV1000s using a 40x oil-immersion lens.

Acknowledgement

The authors would like to thank Greg Jefferis, Phillip Schlegel, Alex Bates, Marta Costa, Fiona Love and Ruairi Roberts for providing access to tracings of PNs in the FAFB dataset, as well as Jay Milam for assistance with confocal scans and Tom Kazimiers, Andrew Champions, Chris Barnes and Albert Cardona for CATMAID support and Mert Erginkaya for assistance with tracing review. We would also like to thank Philipp Schlegel for developing the software Pymaid and the Python code to analyze the CSDn reconstruction and Kevin Daly for useful comments on the manuscript. This work was supported by a Whitehall Foundation Grant and an NIH R21 to QG, an NIH DC 016293 to AMD and QG, and Georgia Gwinnett College VPASA Seed Fund partially supported CG. The contributions of AMD and KEC in this project were supported in part by the Janelia Visiting Scientist Program.

Competing interests

The authors declare no competing interests.

Figure legends

Figure 1. Olfactory stimulation inhibits CSDn processes in the AL. (*A*) (*A*) A single CSDn expressing GFP shows processes in both the AL and the LH. White = GFP expression, blue = neuropil labeling via N-cadherin immunocytochemistry. Scale bar = 50um. (*B*) Background fluorescence from GCaMP6s expression in CSDn neurites in the AL. L = lateral, P = posterior. The same notation is used in subsequent figures (*C*) Odor-evoked changes in calcium (ΔF/F) levels in the AL processes of the CSDn. Cooler colors (blue) represent decreases in calcium levels and warmer (red) colors show increases in calcium. Color bar values are set to the maximum and minimum pixel value across all odors. Images are generated from volumetric stacks by first averaging the z-stack for each volume during the trial to generate 2D frames, and then averaging across 3 frames during the peak of the odor response. Each odor was presented 3 – 4 times and final image is the mean frame of these trials. Odors are diluted 10^{-2} in paraffin oil (PA), which serves as a solvent control. Images are scaled and oriented as in *B*. (*D*) Odor responses ranked according to the strength of the observed inhibition (n = 10). From left to right, p = 0.06, p = 0.81, p = 0.51, p = 0.0097, p = 0.0022, p = 0.0052, p = 0.0051, p = 0.0012, p = 0.0017, p = 1.82×10^{-4}, p = 2.95×10^{-6}, p = 2.50×10^{-5}. *Student's t-test*. * = p < 0.01, ** = p < 0.001. (*E*) Odor-evoked inhibition observed in the CSDn soma via whole-cell patch-clamp recording. (*F*) Principal component analysis performed on the spatial pattern at the peak of the odor responses. White outline represents an ROI used to mask pixels outside of the AL for PCA. The first three PCs are shown. A structured response is only observed in PC1. Images are scaled and oriented as in *B*. The variance and SEM explained by PCs 1 – 3 are 60.3 ± 2.2%, 6.3 ± 0.4%, and 6.1 ± 0.3%, respectively.

Figure 1 – figure supplement 1. CSDn calcium responses in the AL rescaled to emphasize excitation. The same data as Figure 1C are displayed but with a rescaled color bar.

Figure 1 – Video 1. Olfactory stimulation inhibits serotonergic CSDn neurites in the antennal lobe. *Left.* Basal GCaMP6s fluorescence in the neurites of the CSDn. *Right*. The ΔF/F response of the CSDn neurite seen on the left. Scale bar = 20 μm. Color indicates percent change in ΔF/F.

Figure 2. Olfactory stimulation excites CSDn processes in the LH. (*A*) Background fluorescence from GCaMP6s expression in CSDn neurites in the LH. (*B*) Odor-evoked changes in calcium observed in CSDn processes in the LH. Odor scale bar = 20 μm (*C*) Principal component analysis performed on the spatial pattern at the peak of the odor responses for a sample preparation. White outline represents an ROI used for masking during PCA.The first three PCs are shown. A structured response is observed in each PC. Images are scaled as in *B*. The variance and SEM explained by PCs 1 – 3 are 45.2 $\pm$ 2.6%, 12.4 $\pm$ 0.9%, and 8.6 $\pm$ 0.6%. (*D*) The coefficient of variation for odor responses in the AL and LH. n = 10, AL and n = 8, LH. p = 0.0021, Student's t-test. The CV was calculated for each pixel in the odor response images and averaged across pixels for each preparation. (*E*) A comparison of the time series of ΔF/F responses in the AL and LH to a single odorant, p-cresol. The response is the averaged across 10 animals in the AL and 8 in the LH. Error bars represent SEM.

Figure 2 – figure supplement 1. Activation patterns in the LH are similar across preparations. (*A*) The first 3 PC images are shown for 3 sample preparations (of our total data set of 8 animals). White ROI demarcates the boundaries of the LH. Note that for each preparation, PC1 shows activation of a core region of the LH, PC2 shows activation in outer shell region, and PC3 shows inhibition in the central core of the LH. (*B*) Differences in precise branching patterns of the CSDn across flies may contribute to the variability in odor responses across flies. Three CDNs are labeled in different flies and the exact branching pattern is unique to each animal.

Figure 2 – figure supplement 2. Olfactory stimulation activates presynaptic release sites in CSDn terminals in the LH. (*A*) A schematic of the *Drosophila* brain and the region of imaging. (*B*) Odor responses measured with sytGCaMP6s revealing activation of presynaptic release sites in one preparation. Similar results were obtained in 8 preparations in total. (*C*) Skeleton of the CSDn reconstruction in the lateral horn. Blue markers represent postsynaptic sites while red markers represent presynaptic sites. Scale bar = 50um. (*D* - *E*) Insets from (*A*) highlighting the proximity of presynaptic and postsynaptic sites. (*F*) A histogram showing the distribution of distances to the closest postsynaptic site to each presynaptic site in the CSDn. Because pre- and postsynaptic sites occur in such close proximity, it is possible that calcium entry from postsynaptic receptors may directly cause presynaptic release. Additionally, overexpression of the sytGCaMP6s at presynaptic release sites could potentially allow the sensor to report calcium entry at postsynaptic receptors.

Figure 2 – Video 1. Olfactory stimulation excites serotonergic CSDn neurites in the lateral horn. *Left.* Basal GCaMP6s fluorescence in the neurites of the CSDn. *Right*. The ΔF/F response of the CSDn neurite seen on the left. Scale bar = 20 μm. Color indicates percent change in ΔF/F.

Figure 3. Projection neurons shape CSDn responses in the LH via direct synaptic input. (*A*) A cross correlation of the spatial profile of odor responses in CSDn LH processes. (*B*) Clustering analysis using the Euclidean distance between correlations for odor pairs from (*A*). (*C*) Regression analysis on correlation distances between odor responses in processes of the CSDn and PN axons in the LH ($R^2 = 0.77$, $p = 4.07*10^{-22}$, n = 10 preparations for CSDn and n = 5 for PN responses). Distances were normalized to the max distance observed for CSDns and PNs. The 66 open circles represent the distances for each odor pair (12 odors and 66 pairwise comparisons). PN odor responses where measured using GCaMP6s and the GH146-Gal4 promoter. (*D – F*) GRASP images showing direct synaptic input from PNs onto CSDn terminals. Green = 5-HT antibody to label CSDn processes, yellow = syb-GFP subunits 1-10 expressed in PN axons, magenta = syb-GRASP labeling of synapses. Scale bars = 20 μm. (*G*) EM image of a direct VA1d PN synapse onto a CSDn neurite in the AL Scale bar = 500nm. (*H*) EM reconstruction of the CSDn (black) arbors in the LH (grey boundary). Location of individual PN synapses onto the CSDn are marked in green. Scale bar = 25um. (*I*) A total count of PN synapses onto the CSDn in the LH separated by glomerular identity. Glomeruli are listed above and below bars for clarity. DM2 is represented twice as two synapses arose from one DM2 PN and another synapse was identified from another DM2 PN. Counts taken from 1 female brain.

Figure 3 – figure supplement 1. The axons of projection neurons in the LH have odor specific patterns of activation. (*A*) Calcium responses of PN axons in the LH revealed with GCaMP6s and the GH146-Gal4 promoter. PCA analysis shows several unique patterns of activation are required to explain the variance in the data set of odor response. (*B*) Clustering analysis on the Euclidean distance of correlations across odors in PN responses in the LH (n = 5).

Figure 4. AL inhibition suppresses CSDn responses in the LH. (*A*) Morphological EM reconstruction of the CSDn arborizations used for a biophysical model consisting of 6056 compartments. (*B*) Somatic membrane potential changes in response to a white-noise current injection during an *in vivo* CSDn recording compared to responses of a passive compartmental model, to the same stimulus, fitted by optimizing three anatomical parameters, C_m (μF/cm^2), g_{leak} (S/cm^2), and R_a (Ωcm), (*C*) An example of a model with well-fit somatic responses where a

hyperpolarizing current injection in the AL resulted in highly localized voltage changes in AL only. A time series of voltage responses are shown for the soma, AL, and LH as gray traces near those structures. $C_m = 4.8$, $g_{leak} = 3094.3$, and $R_a = 149.0183$. Horizontal scale bar = 5 ms and vertical scale bar = 5 mV. (*D*) A similar model where injection of the current in the AL causes a voltage change throughout a greater portion of the AL. $C_m = 4.8$, $g_{leak} = 2911.3$, and $R_a = 28.83$. Scale bars as in *C*. (*E*) A sample model where current injection into the AL causes both somatic and LH voltage changes. $C_m = 1.8$,$_w$ $g_{leak} = 77.33$, and $R_a = 0.12$. Scale bars as in *C*. (*F*) The proportion of voltage signal observed in the LH, AL, and cell body (CB) when voltage changes are induced in each region. The same model as in panel *E* was used to generate the data. *Left*, voltage steps are induced into the AL and voltage deflections are reported in the LH and CB. *Right*, voltage steps are induced in the LH and their effects are measured in the AL and CB. Horizontal scale bar = 10 ms and vertical scale bar = 10 mV. (*G*) A 2P image of basal GCaMP6s signal showing the effects of laser ablation in the CSDn LH neurite. (*H*) Basal GCaMP6s signals remain in the LH after laser ablation. (*I*) ΔF/F responses of CSDn neurites in the LH to a set of odorants before and after laser ablation. (*J*) A times series of the changes in calcium levels in response to odorants in (*I*). (*K*) *Left*, quantification of odor response amplitudes in CSDn LH neurites before and after laser ablation. *Right*, control responses when the contralateral processes of the CSDn where ablated. *Left column, top to bottom*, p = 0.0187, p = 0.0067, p = 0.0154; *Right column, top to bottom* p = 0.2298, p = 0.8958, p = 0.1611. * = p < 0.05, ** = p < 0.01, n.s. = not significant and p > 0.05, paired Student's t-tests.

Figure 4 – figure supplement 1. Sampling strategy for measuring CSDn axon radius. (*A*) Reconstruction of the CSDn skeleton from the whole brain EM volume. Thickened processes indicate individual sampling locations from which 20-50 measures were taken. Inset box or brackets indicate individual regions from which multiple samples were taken and shown in more detail in subsequent panels. (*B*) Axon radius sampling locations from the main branch of the CSDn. (*C*) Sampling locations from the CSDn process passing through the superior-medial protocerebrum (SMP) to the LH. (*D*) Sampling locations from 6 separate branches of the CSDn in the LH (boundary shaded in grey).

Figure 4 – figure supplement 2. cVA excites CSDn processes in the lateral horn. (*A*) Experimental approach as in Figure *4G -K*. *Top*, basal fluorescence of GCaMP6s signal before and after ablation of the processes connecting the AL and LH. *Bottom*, ΔF/F responses of CSDn neurites in the LH to cVA. (*B*) *Top*, a time course of the calcium response to cVA before and

after laser ablation. *Bottom*, quantification of the data in *A* and *B* for ipsilateral and contralateral control lesion experiments.

Supplementary File 1. A table of the parameters and their values used to construct the passive compartmental model of the CSDn.

References

Berke, J.D., 2018. What does dopamine mean? Nat Neurosci 1–7. doi:10.1038/s41593-018-0152-y

Briggman, K.L., Kristan, W.B., Jr., 2008. Multifunctional pattern-generating circuits. Annu Rev Neurosci 31, 271–294.

Carnevale, N.T., Hines, M.L., 2006. The NEURON Book. Cambridge University Press, Cambridge, UK.

Charnay, Y., Léger, L., 2010. Brain serotonergic circuitries. Dialogues Clin Neurosci 12, 471–487.

Chen, T.-W., Wardill, T.J., Sun, Y., Pulver, S.R., Renninger, S.L., Baohan, A., Schreiter, E.R., Kerr, R.A., Orger, M.B., Jayaraman, V., Looger, L.L., Svoboda, K., Kim, D.S., 2013. Ultrasensitive fluorescent proteins for imaging neuronal activity. Nature 499, 295–300. doi:10.1038/nature12354

Coates, K.E., Majot, A.T., Zhang, X., Michael, C.T., Spitzer, S.L., Gaudry, Q., Dacks, A.M., 2017. Identified Serotonergic Modulatory Neurons Have Heterogeneous Synaptic Connectivity within the Olfactory System of Drosophila. Journal of Neuroscience 37, 7318–7331. doi:10.1523/JNEUROSCI.0192-17.2017

Cohn, R., Morantte, I., Ruta, V., 2015. Coordinated and Compartmentalized Neuromodulation Shapes Sensory Processing in Drosophila. Cell 163, 1742–1755. doi:10.1016/j.cell.2015.11.019

Dacks, A.M., Christensen, T.A., Hildebrand, J.G., 2006. Phylogeny of a serotonin-immunoreactive neuron in the primary olfactory center of the insect brain. The Journal of Comparative Neurology 498, 727–746. doi:10.1002/cne.21076

Dankoski, E.C., Wightman, R.M., 2013. Monitoring serotonin signaling on a subsecond time scale. Front Integr Neurosci 7, 44. doi:10.3389/fnint.2013.00044

de Belle, J.S., Heisenberg, M., 1994. Associative odor learning in Drosophila abolished by chemical ablation of mushroom bodies. Science 263, 692–695.

Egashira, N., Mishima, K., Katsurabayashi, S., Yoshitake, T., Matsumoto, Y., Ishida, J., Yamaguchi, M., Iwasaki, K., Fujiwara, M., 2002. Involvement of 5-hydroxytryptamine neuronal system in Delta(9)-tetrahydrocannabinol-induced impairment of spatial memory. Eur. J. Pharmacol. 445, 221–229.

Feinberg, E.H., VanHoven, M.K., Bendesky, A., Wang, G., Fetter, R.D., Shen, K., Bargmann, C.I., 2008. GFP Reconstitution Across Synaptic Partners (GRASP) Defines Cell Contacts and Synapses in Living Nervous Systems. Neuron 57, 353–363. doi:10.1016/j.neuron.2007.11.030

Floresco, S.B., Yang, C.R., Phillips, A.G., Blaha, C.D., 1998. Basolateral amygdala stimulation evokes glutamate receptor-dependent dopamine efflux in the nucleus accumbens of the anaesthetized rat. Eur. J. Neurosci. 10, 1241–1251.

Gagnon, D., Parent, M., 2014. Distribution of VGLUT3 in highly collateralized axons from the rat dorsal raphe nucleus as revealed by single-neuron reconstructions. PLoS One 9, e87709. doi:10.1371/journal.pone.0087709

Gaudry, Q., 2018. Serotonergic Modulation of Olfaction in Rodents and Insects. Yale J Biol Med 91, 23–32.

Gracia-Llanes, F.J., Blasco-Ibáñez, J.M., Nácher, J., Varea, E., Liberia, T., Martínez, P., Martínez-Guijarro, F.J., Crespo, C., 2010. Synaptic connectivity of serotonergic axons in the olfactory glomeruli of the rat olfactory bulb. Neuroscience 169, 770–780. doi:10.1016/j.neuroscience.2010.05.034

Hamid, A.A., Pettibone, J.R., Mabrouk, O.S., Hetrick, V.L., Schmidt, R., Vander Weele, C.M., Kennedy, R.T., Aragona, B.J., Berke, J.D., 2015. Mesolimbic dopamine signals the value of work. Nat Neurosci 19, 117–126. doi:10.1038/nn.4173

Hill, E.S., Iwano, M., Gatellier, L., Kanzaki, R., 2002. Morphology and physiology of the serotonin-immunoreactive putative antennal lobe feedback neuron in the male silkmoth Bombyx mori. Chemical senses 27, 475–483.

695 Hong, E.J., Wilson, R.I., 2015. Simultaneous encoding of odors by channels with diverse sensitivity to
696 inhibition. Neuron 85, 573–589. doi:10.1016/j.neuron.2014.12.040
697 Hornung, J.-P., 2003. The human raphe nuclei and the serotonergic system. J. Chem. Neuroanat. 26,
698 331–343. doi:10.1016/j.jchemneu.2003.10.002
699 Huang, Z., Thiebaud, N., Fadool, D.A., 2017. Differential serotonergic modulation across the main and
700 accessory olfactory bulbs. J Physiol (Lond) 595, 3515–3533. doi:10.1113/JP273945
701 Ikemoto, S., 2007. Dopamine reward circuitry: Two projection systems from the ventral midbrain to the
702 nucleus accumbens–olfactory tubercle complex. Brain Research Reviews 56, 27–78.
703 doi:10.1016/j.brainresrev.2007.05.004
704 Jacob, S.N., Nienborg, H., 2018. Monoaminergic Neuromodulation of Sensory Processing. Front Neural
705 Circuits 12, 70–17. doi:10.3389/fncir.2018.00051
706 Jefferis, G., Potter, C.J., Chan, A.M., Marin, E.C., Rohlfing, T., Maurer, C.R., Luo, L., 2007. Comprehensive
707 maps of Drosophila higher olfactory centers: spatially segregated fruit and pheromone
708 representation. Cell 128, 1187–1203. doi:10.1016/j.cell.2007.01.040
709 Jones, J.L., Day, J.J., Aragona, B.J., Wheeler, R.A., Wightman, R.M., Carelli, R.M., 2010. Basolateral
710 amygdala modulates terminal dopamine release in the nucleus accumbens and conditioned
711 responding. Biological Psychiatry 67, 737–744. doi:10.1016/j.biopsych.2009.11.006
712 Jones, P.W., Gabbiani, F., 2010. Synchronized neural input shapes stimulus selectivity in a collision-
713 detecting neuron. Curr Biol 20, 2052–2057. doi:10.1016/j.cub.2010.10.025
714 Katz, P.S., 1995. Intrinsic and extrinsic neuromodulation of motor circuits. Current Opinion in
715 Neurobiology 5, 799–808.
716 Kloppenburg, P., Mercer, A.R., 2008. Serotonin modulation of moth central olfactory neurons. Annu.
717 Rev. Entomol. 53, 179–190. doi:10.1146/annurev.ento.53.103106.093408
718 Koren, D., Grove, J.C.R., Wei, W., 2017. Cross-compartmental Modulation of Dendritic Signals for Retinal
719 Direction Selectivity. Neuron 95, 914–927.e4. doi:10.1016/j.neuron.2017.07.020
720 Lammel, S., Hetzel, A., Häckel, O., Jones, I., Liss, B., Roeper, J., 2008. Unique Properties of
721 Mesoprefrontal Neurons within a Dual Mesocorticolimbic Dopamine System. Neuron 57, 760–773.
722 doi:10.1016/j.neuron.2008.01.022
723 Lecoq, J., Savall, J., Vučinić, D., Grewe, B.F., Kim, H., Li, J.Z., Kitch, L.J., Schnitzer, M.J., 2014. Visualizing
724 mammalian brain area interactions by dual-axis two-photon calcium imaging. Nat Neurosci 17,
725 1825–1829. doi:10.1038/nn.3867
726 Lizbinski, K.M., Dacks, A.M., 2017. Intrinsic and Extrinsic Neuromodulation of Olfactory Processing. Front
727 Cell Neurosci 11, 424. doi:10.3389/fncel.2017.00424
728 Lottem, E., Lörincz, M.L., Mainen, Z.F., 2016. Optogenetic Activation of Dorsal Raphe Serotonin Neurons
729 Rapidly Inhibits Spontaneous But Not Odor-Evoked Activity in Olfactory Cortex. Journal of
730 Neuroscience 36, 7–18. doi:10.1523/JNEUROSCI.3008-15.2016
731 Macpherson, L.J., Zaharieva, E.E., Kearney, P.J., Alpert, M.H., Lin, T.-Y., Turan, Z., Lee, C.-H., Gallio, M.,
732 2015. Dynamic labelling of neural connections in multiple colours by trans-synaptic fluorescence
733 complementation. Nature Communications 6, 10024–9. doi:10.1038/ncomms10024
734 Melzer, S., Michael, M., Caputi, A., Eliava, M., Fuchs, E.C., Whittington, M.A., Monyer, H., 2012. Long-
735 range-projecting GABAergic neurons modulate inhibition in hippocampus and entorhinal cortex.
736 Science 335, 1506–1510. doi:10.1126/science.1217139
737 Miller, R.J., 1998. Presynaptic receptors. Annual Review of Pharmacology and Toxicology 38, 201–227.
738 doi:10.1146/annurev.pharmtox.38.1.201
739 Min, S., Ai, M., Shin, S.A., Suh, G.S.B., 2013. Dedicated olfactory neurons mediating attraction behavior
740 to ammonia and amines in Drosophila. Proceedings of the National Academy of Sciences.
741 doi:10.1073/pnas.1215680110

742 Nikitin, E.S., Balaban, P.M., Kemenes, G., 2013. Nonsynaptic Plasticity Underlies a Compartmentalized
743 Increase in Synaptic Efficacy after Classical Conditioning. CURBIO 23, 614–619.
744 doi:10.1016/j.cub.2013.02.048
745 Nunez-Parra, A., Maurer, R.K., Krahe, K., Smith, R.S., Araneda, R.C., 2013. Disruption of centrifugal
746 inhibition to olfactory bulb granule cells impairs olfactory discrimination. Proceedings of the
747 National Academy of Sciences 110, 14777–14782. doi:10.1073/pnas.1310686110
748 Ogawa, S.K., Cohen, J.Y., Hwang, D., Uchida, N., Watabe-Uchida, M., 2014. Organization of
749 Monosynaptic Inputs to the Serotonin and Dopamine Neuromodulatory Systems. CellReports 8,
750 1105–1118. doi:10.1016/j.celrep.2014.06.042
751 Otazu, G.H., Chae, H., Davis, M.B., Albeanu, D.F., 2015. Cortical Feedback Decorrelates Olfactory Bulb
752 Output in Awake Mice. Neuron 86, 1461–1477. doi:10.1016/j.neuron.2015.05.023
753 Padmanabhan, K., Osakada, F., Tarabrina, A., Kizer, E., Callaway, E.M., Gage, F.H., Sejnowski, T.J., 2019.
754 Centrifugal Inputs to the Main Olfactory Bulb Revealed Through Whole Brain Circuit-Mapping.
755 Front. Neuroanat. 12, 413. doi:10.3389/fnana.2018.00115
756 Petzold, G.C., Hagiwara, A., Murthy, V.N., 2009. Serotonergic modulation of odor input to the
757 mammalian olfactory bulb. Nat Neurosci 12, 784–791. doi:10.1038/nn.2335
758 Pollak Dorocic, I., Fürth, D., Xuan, Y., Johansson, Y., Pozzi, L., Silberberg, G., Carlén, M., Meletis, K., 2014.
759 A whole-brain atlas of inputs to serotonergic neurons of the dorsal and median raphe nuclei.
760 Neuron 83, 663–678. doi:10.1016/j.neuron.2014.07.002
761 Ranganathan, G.N., Apostolides, P.F., Harnett, M.T., Xu, N.-L., Druckmann, S., Magee, J.C., 2018. Active
762 dendritic integration and mixed neocortical network representations during an adaptive sensing
763 behavior. Nat Neurosci 1–13. doi:10.1038/s41593-018-0254-6
764 Rothermel, M., Carey, R.M., Puche, A., Shipley, M.T., Wachowiak, M., 2014. Cholinergic inputs from
765 Basal forebrain add an excitatory bias to odor coding in the olfactory bulb. Journal of Neuroscience
766 34, 4654–4664. doi:10.1523/JNEUROSCI.5026-13.2014
767 Roy, B., Singh, A.P., Shetty, C., Chaudhary, V., North, A., Landgraf, M., Vijayraghavan, K., Rodrigues, V.,
768 2007. Metamorphosis of an identified serotonergic neuron in the Drosophila olfactory system.
769 Neural Dev 2, 1. doi:10.1186/1749-8104-2-20
770 Saalfeld, S., Cardona, A., Hartenstein, V., Tomancak, P., 2009. CATMAID: collaborative annotation toolkit
771 for massive amounts of image data. Bioinformatics 25, 1984–1986.
772 doi:10.1093/bioinformatics/btp266
773 Sasaki, K., Due, M.R., Jing, J., Weiss, K.R., 2007. Feeding CPG in Aplysia directly controls two distinct
774 outputs of a compartmentalized interneuron that functions as a CPG element. Journal of
775 Neurophysiology 98, 3796–3801. doi:10.1152/jn.00965.2007
776 Schlicker, E., Classen, K., Göthert, M., 1984. Gabab Receptor-Mediated Inhibition of Serotonin Release in
777 the Rat-Brain. Naunyn Schmiedebergs Arch. Pharmacol. 326, 99–105.
778 Schneider-Mizell, C.M., Gerhard, S., Longair, M., Kazimiers, T., Li, F., Zwart, M.F., Champion, A., Midgley,
779 F.M., Fetter, R.D., Saalfeld, S., Cardona, A., 2016. Quantitative neuroanatomy for connectomics in
780 Drosophila. Elife 5. doi:10.7554/eLife.12059
781 Schwarz, L.A., Luo, L., 2015. Organization of the locus coeruleus-norepinephrine system. Curr Biol 25,
782 R1051–R1056. doi:10.1016/j.cub.2015.09.039
783 Seki, Y., Dweck, H.K.M., Rybak, J., Wicher, D., Sachse, S., Hansson, B.S., 2017. Olfactory coding from the
784 periphery to higher brain centers in the Drosophila brain 1–20. doi:10.1186/s12915-017-0389-z
785 Singh, A.P., Das, R.N., Rao, G., Aggarwal, A., Diegelmann, S., Evers, J.F., Karandikar, H., Landgraf, M.,
786 Rodrigues, V., Vijayraghavan, K., 2013. Sensory neuron-derived eph regulates glomerular arbors and
787 modulatory function of a central serotonergic neuron. PLoS Genet 9, e1003452.
788 doi:10.1371/journal.pgen.1003452

789 Sofroniew, N.J., Flickinger, D., King, J., Svoboda, K., 2016. A large field of view two-photon mesoscope
790 with subcellular resolution for in vivo imaging. Elife 5, 413. doi:10.7554/eLife.14472
791 Sparta, D.R., Stuber, G.D., 2014. Cartography of Serotonergic Circuits. Neuron 83, 513–515.
792 doi:10.1016/j.neuron.2014.07.030
793 Stirman, J.N., Smith, I.T., Kudenov, M.W., Smith, S.L., 2016. Wide field-of-view, multi-region, two-photon
794 imaging of neuronal activity in the mammalian brain. Nat. Biotechnol. 34, 857–862.
795 doi:10.1038/nbt.3594
796 Strutz, A., Soelter, J., Baschwitz, A., Farhan, A., Grabe, V., Rybak, J., Knaden, M., Schmuker, M., Hansson,
797 B.S., Sachse, S., 2014. Decoding odor quality and intensity in the Drosophila brain. Elife 3, e04147.
798 doi:10.7554/eLife.04147
799 Stuart, G., Spruston, N., Häusser, M., 2016. Dendrites, 3rd ed. Oxford University Press.
800 Sun, X.J., Tolbert, L.P., Hildebrand, J.G., 1993. Ramification pattern and ultrastructural characteristics of
801 the serotonin-immunoreactive neuron in the antennal lobe of the moth Manduca sexta: a laser
802 scanning confocal and electron microscopic study. The Journal of Comparative Neurology 338, 5–
803 16. doi:10.1002/cne.903380103
804 Suzuki, Y., Kiyokage, E., Sohn, J., Hioki, H., Toida, K., 2014. Structural basis for serotonergic regulation of
805 neural circuits in the mouse olfactory bulb. J. Comp. Neurol. 523, 262–280. doi:10.1002/cne.23680
806 Tanaka, N.K., Awasaki, T., Shimada, T., Ito, K., 2004. Integration of Chemosensory Pathways in the
807 Drosophila Second-Order Olfactory Centers. Current Biology 14, 449–457.
808 doi:10.1016/j.cub.2004.03.006
809 Tao, R., Auerbach, S.B., 1995. Involvement of the dorsal raphe but not median raphe nucleus in
810 morphine-induced increases in serotonin release in the rat forebrain. NSC 68, 553–561.
811 Terada, S.-I., Kobayashi, K., Ohkura, M., Nakai, J., Matsuzaki, M., 2018. Super-wide-field two-photon
812 imaging with a micro- optical device moving in post-objective space. Nature Communications 1–14.
813 doi:10.1038/s41467-018-06058-8
814 Thiele, A., Bellgrove, M.A., 2018. Neuromodulation of Attention. Neuron 97, 769–785.
815 doi:10.1016/j.neuron.2018.01.008
816 Threlfell, S., Cragg, S.J., Kalló, I., Turi, G.F., Coen, C.W., Greenfield, S.A., 2004. Histamine H3 receptors
817 inhibit serotonin release in substantia nigra pars reticulata. Journal of Neuroscience 24, 8704–8710.
818 doi:10.1523/JNEUROSCI.2690-04.2004
819 van der Kooy, D., Kuypers, H.G., 1979. Fluorescent retrograde double labeling: axonal branching in the
820 ascending raphe and nigral projections. Science 204, 873–875.
821 Varga, V., Sik, A., Freund, T.F., Kocsis, B., 2002. GABA(B) receptors in the median raphe nucleus:
822 distribution and role in the serotonergic control of hippocampal activity. NSC 109, 119–132.
823 doi:10.1016/S0306-4522(01)00448-1
824 Weissbourd, B., Ren, J., DeLoach, K.E., Guenthner, C.J., Miyamichi, K., Luo, L., 2014. Presynaptic Partners
825 of Dorsal Raphe Serotonergic and GABAergic Neurons. Neuron 83, 645–662.
826 doi:10.1016/j.neuron.2014.06.024
827 Wenk, G.L., 1997. The Nucleus Basalis Magnocellularis Cholinergic System: One Hundred Years of
828 Progress. Neurobiology of Learning and Memory 67, 85–95. doi:10.1006/nlme.1996.3757
829 Xu, L., He, J., Kaiser, A., Gräber, N., Schläger, L., Ritze, Y., Scholz, H., 2016. A Single Pair of Serotonergic
830 Neurons Counteracts Serotonergic Inhibition of Ethanol Attraction in Drosophila. PLoS One 11,
831 e0167518–15. doi:10.1371/journal.pone.0167518
832 Zhang, X., Gaudry, Q., 2016. Functional integration of a serotonergic neuron in the Drosophila antennal
833 lobe. Elife 5, 2435. doi:10.7554/eLife.16836
834 Zheng, Z., Lauritzen, J.S., Perlman, E., Robinson, C.G., Nichols, M., Milkie, D., Torrens, O., Price, J., Fisher,
835 C.B., Sharifi, N., Calle-Schuler, S.A., Kmecova, L., Ali, I.J., Karsh, B., Trautman, E.T., Bogovic, J.A.,
836 Hanslovsky, P., Jefferis, G., Kazhdan, M., Khairy, K., Saalfeld, S., Fetter, R.D., Bock, D.D., 2018. A

Complete Electron Microscopy Volume of the Brain of Adult Drosophila melanogaster. Cell 174, 730–743.e22. doi:10.1016/j.cell.2018.06.019

Figure 1

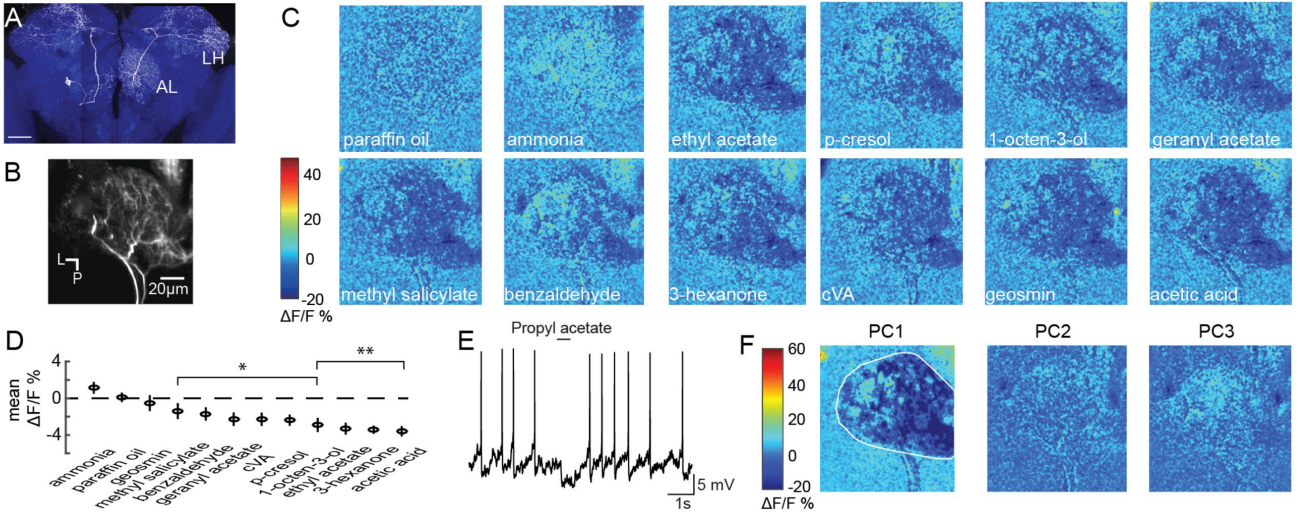
A
LH
AL
B
L
P
20µm
C
paraffin oil
ammonia
ethyl acetate
p-cresol
1-octen-3-ol
geranyl acetate
methyl salicylate
benzaldehyde
3-hexanone
cVA
geosmin
acetic acid
40
20
0
-20
ΔF/F %
D
mean ΔF/F %
4
0
-4
*
**
ammonia
paraffin oil
geosmin
methyl salicylate
benzaldehyde
geranyl acetate
cVA
p-cresol
1-octen-3-ol
ethyl acetate
3-hexanone
acetic acid
E
Propyl acetate
5 mV
1s
F
PC1
PC2
PC3
60
40
20
0
-20
ΔF/F %

Figure 1 figure supplement 1

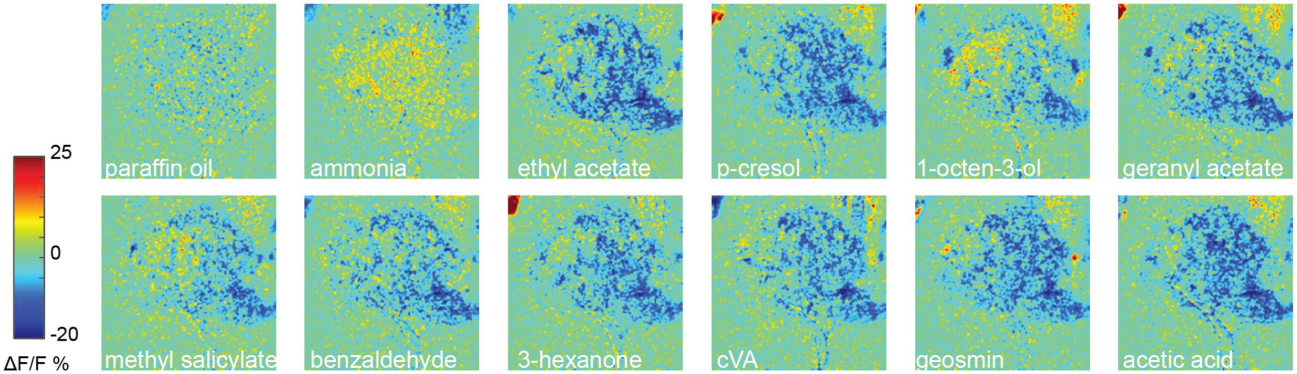

Figure 2

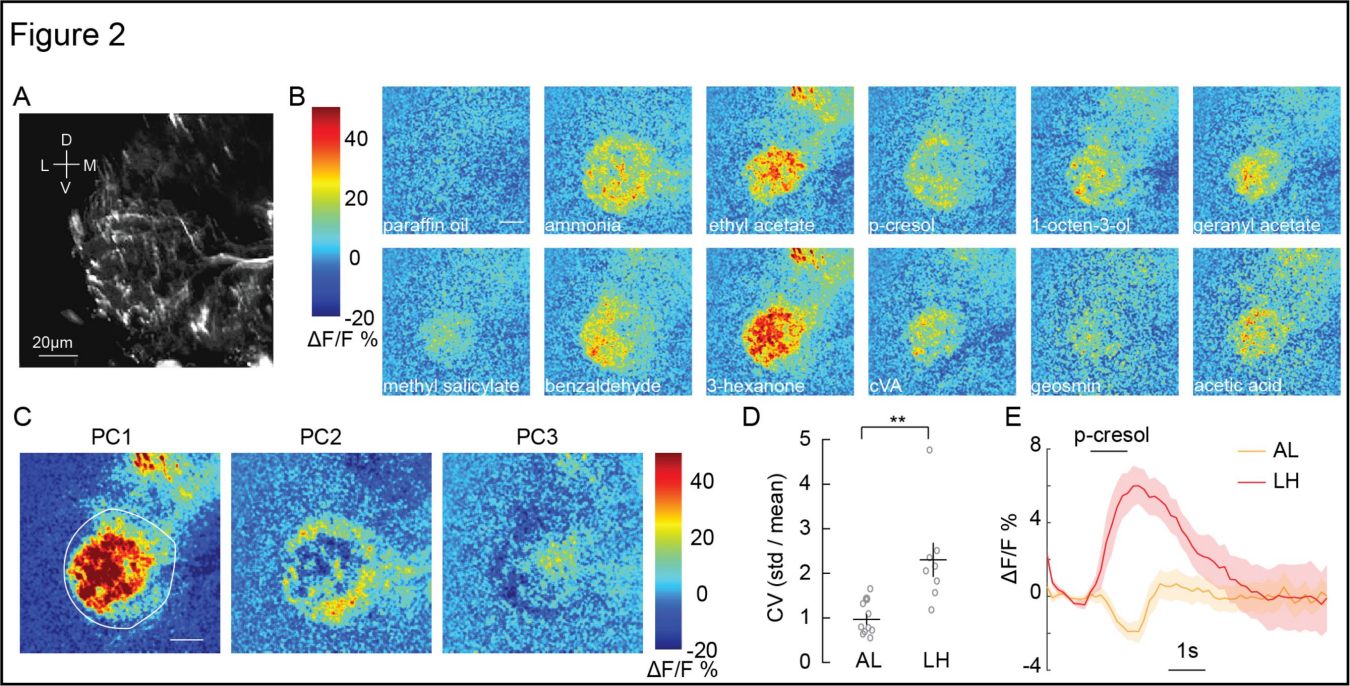
A
D
L
M
V
20μm
B
40
20
0
-20
ΔF/F %
paraffin oil
ammonia
ethyl acetate
p-cresol
1-octen-3-ol
geranyl acetate
methyl salicylate
benzaldehyde
3-hexanone
cVA
geosmin
acetic acid
C
PC1
PC2
PC3
40
20
0
-20
ΔF/F %
D
**
CV (std / mean)
5
4
3
2
1
0
AL
LH
E
p-cresol
AL
LH
8
4
0
-4
ΔF/F %
1s

Figure 2 figure supplement 1

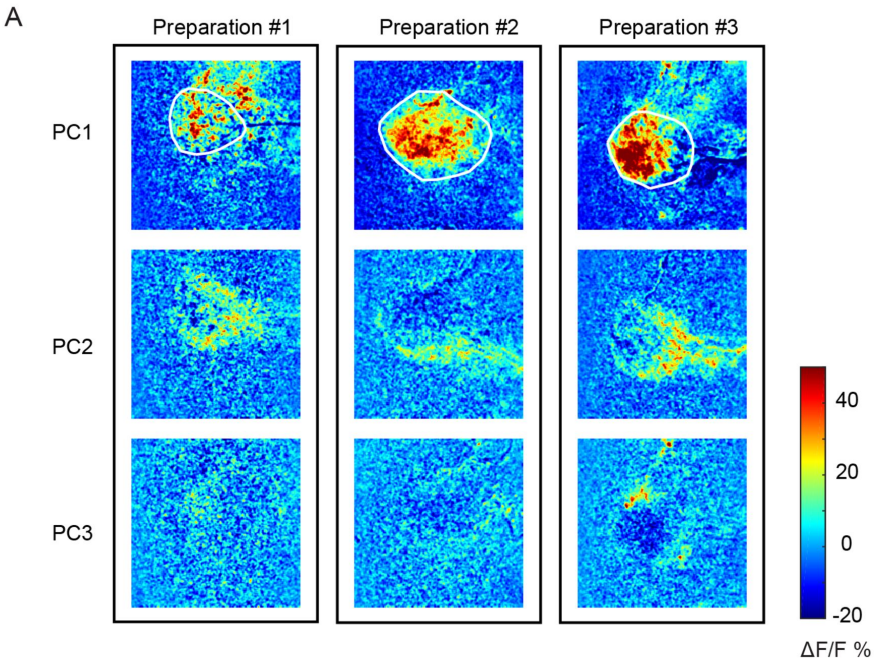

Figure 2 figure supplement 2

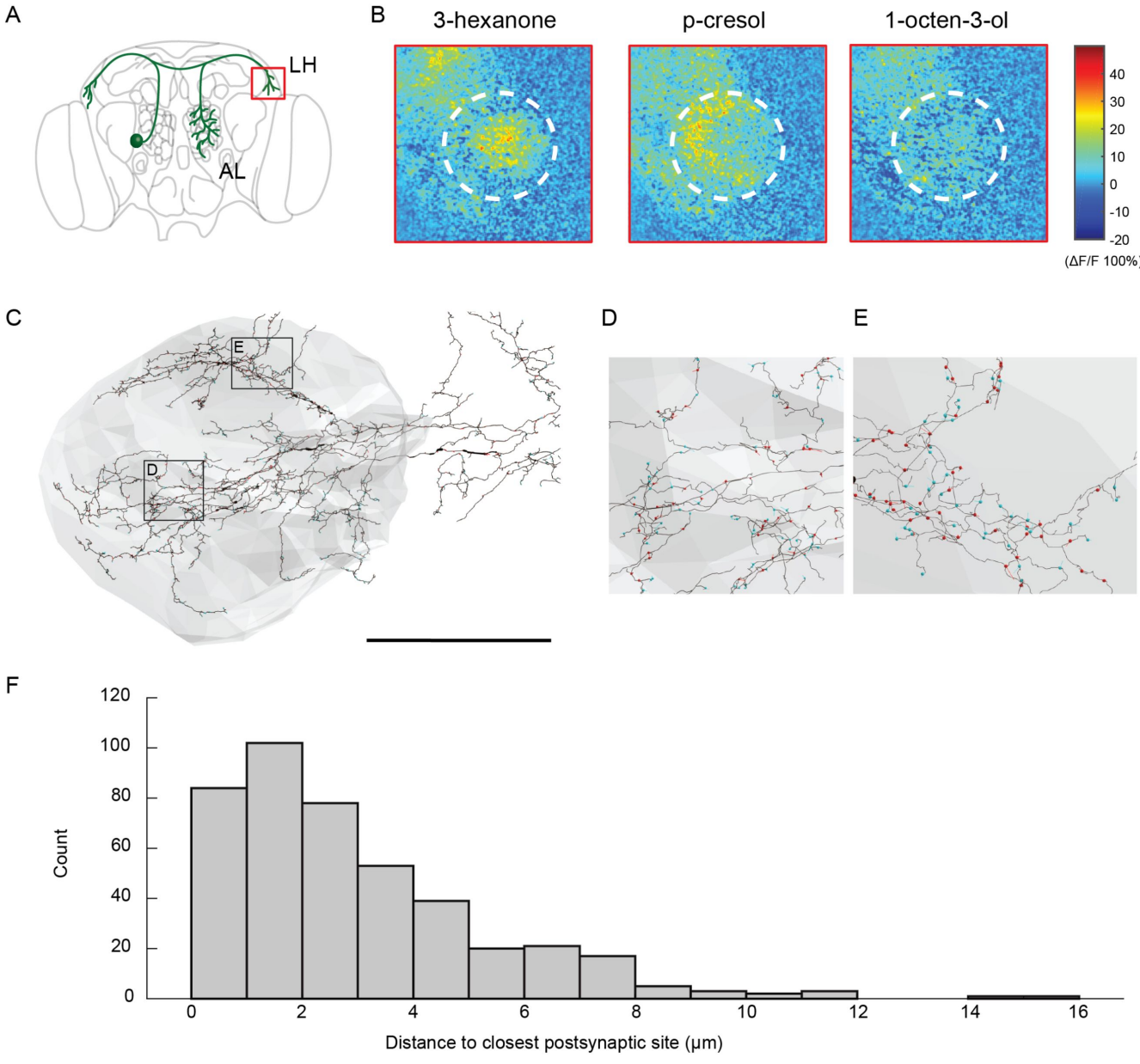

Figure 3

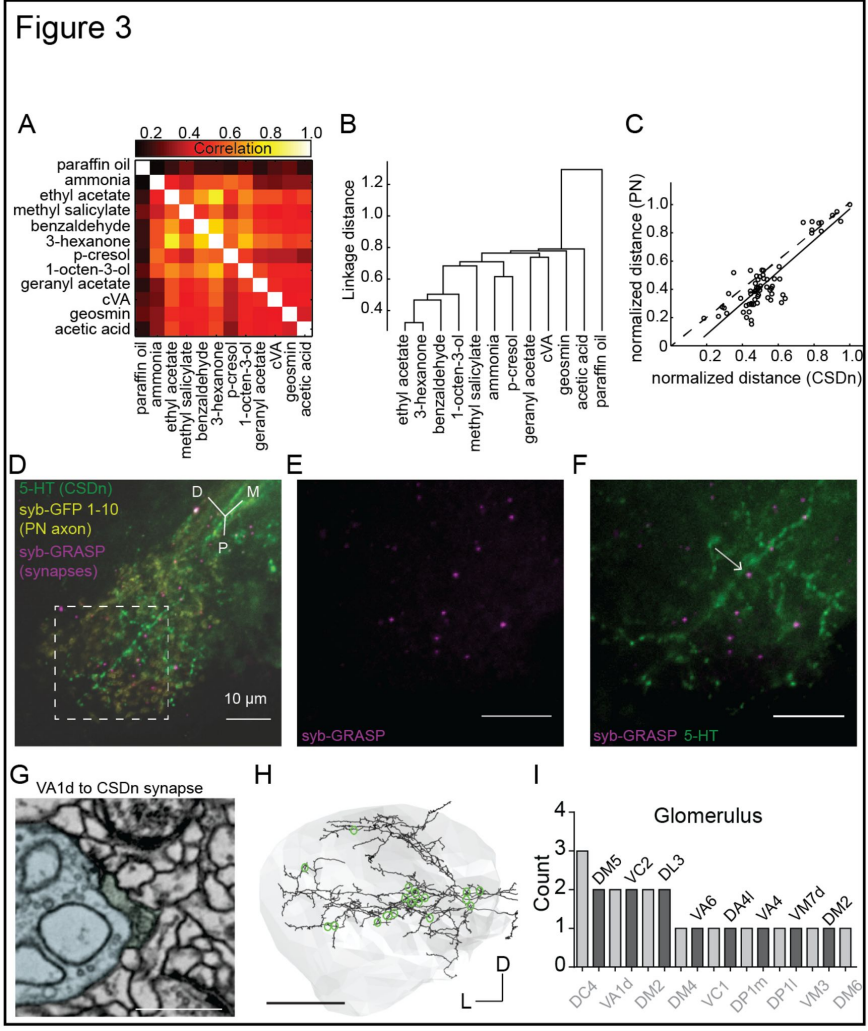
A
0.2 0.4 0.6 0.8 1.0
Correlation
paraffin oil
ammonia
ethyl acetate
methyl salicylate
benzaldehyde
3-hexanone
p-cresol
1-octen-3-ol
geranyl acetate
cVA
geosmin
acetic acid
B
Linkage distance
1.2
1.0
0.8
0.6
0.4
ethyl acetate
3-hexanone
benzaldehyde
1-octen-3-ol
methyl salicylate
ammonia
p-cresol
geranyl acetate
cVA
geosmin
acetic acid
paraffin oil
C
normalized distance (PN)
normalized distance (CSDn)
1.0
0.8
0.6
0.4
0.2
0
0.2 0.4 0.6 0.8 1.0
D
5-HT (CSDn)
syb-GFP 1-10
(PN axon)
syb-GRASP
(synapses)
D
M
P
10 µm
E
syb-GRASP
F
syb-GRASP 5-HT
G
VA1d to CSDn synapse
H
D
L
I
Glomerulus
Count
4
3
2
1
0
DM5
VC2
DL3
VA6
DA4l
VA4
VM7d
DM2
DC4
VA1d
DM2
DM4
VC1
DP1m
DP1l
VM3
DM6

Figure 3 figure supplement 1

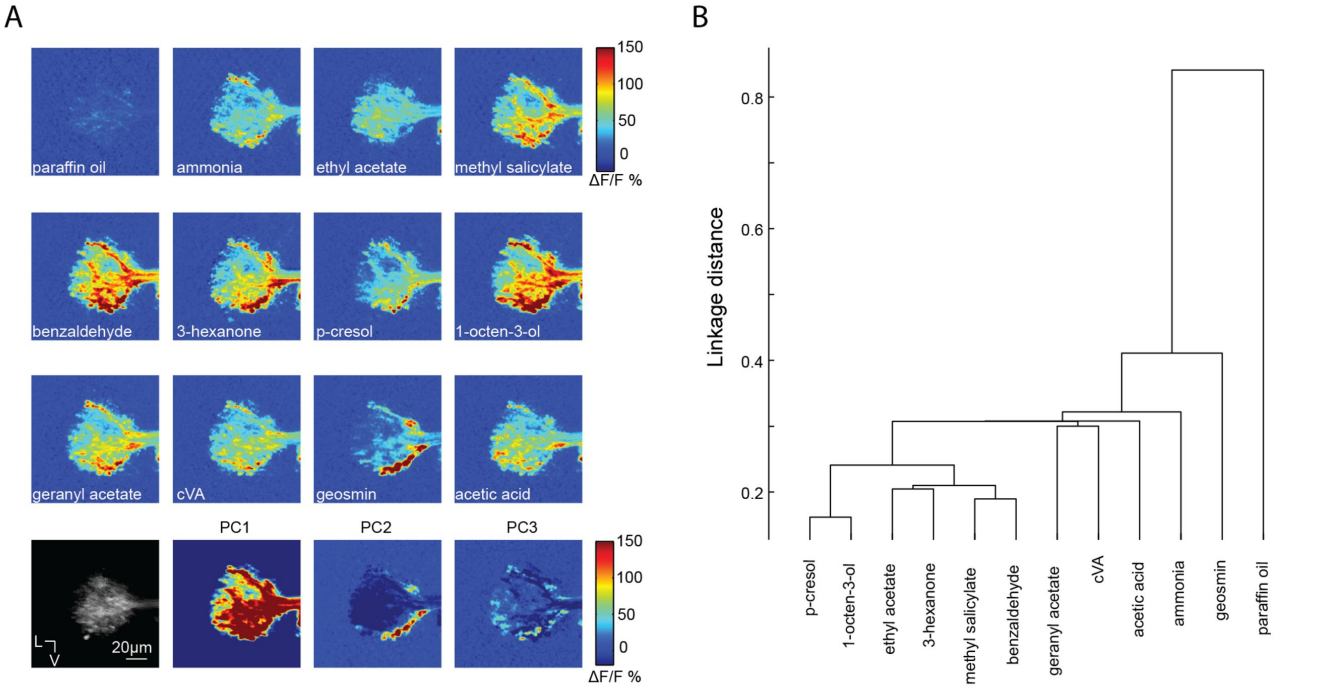

Figure 4

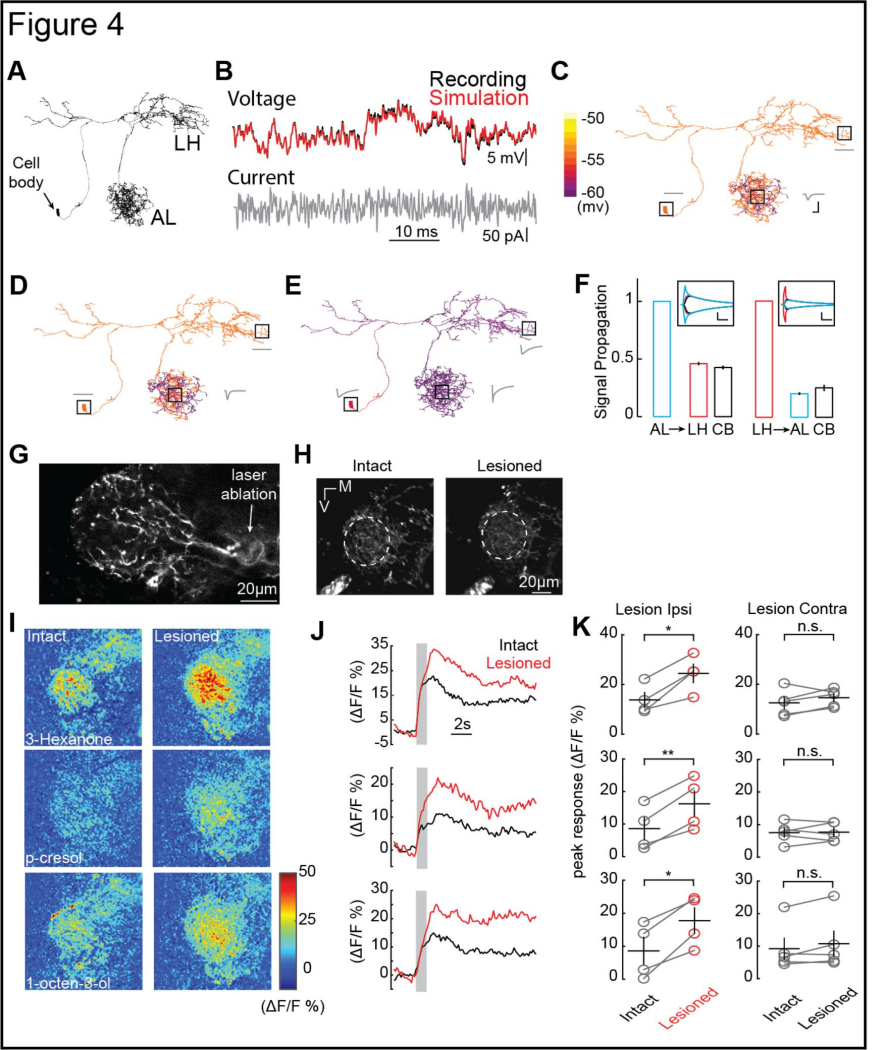
A
Cell body
LH
AL
B
Voltage
Recording
Simulation
5 mV
Current
10 ms
50 pA
C
-50
-55
-60
(mv)
D
E
F
Signal Propagation
1
0.5
0
AL→LH CB
LH→AL CB
G
laser ablation
20μm
H
Intact
Lesioned
M
V
20μm
I
Intact
Lesioned
3-Hexanone
p-cresol
1-octen-3-ol
50
25
0
(ΔF/F %)
J
Intact
Lesioned
(ΔF/F %)
2s
K
Lesion Ipsi
Lesion Contra
peak response (ΔF/F %)
*
**
n.s.
Intact
Lesioned

Figure 4 figure supplement 1

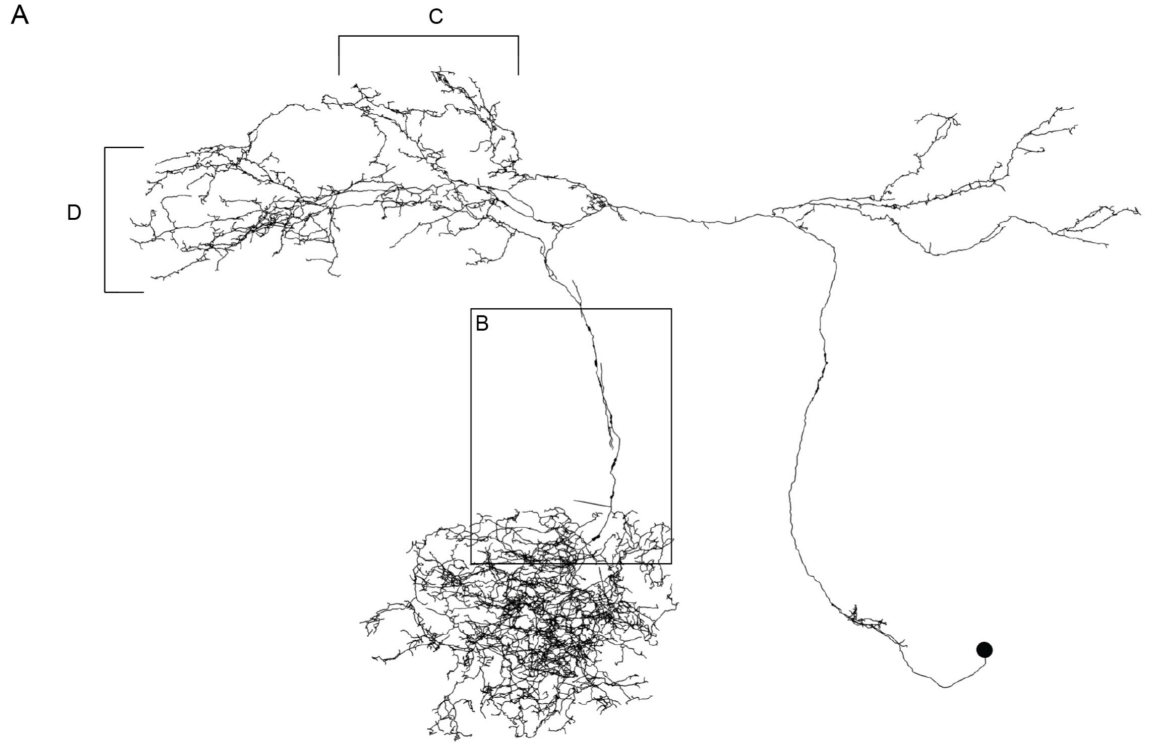

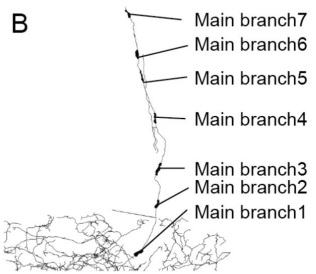

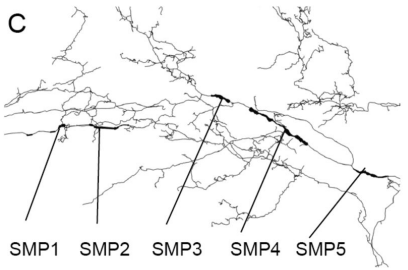

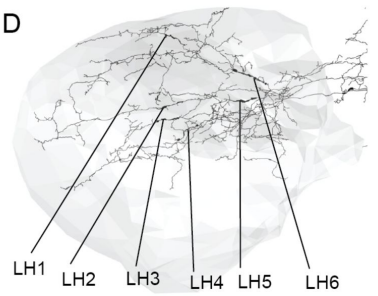
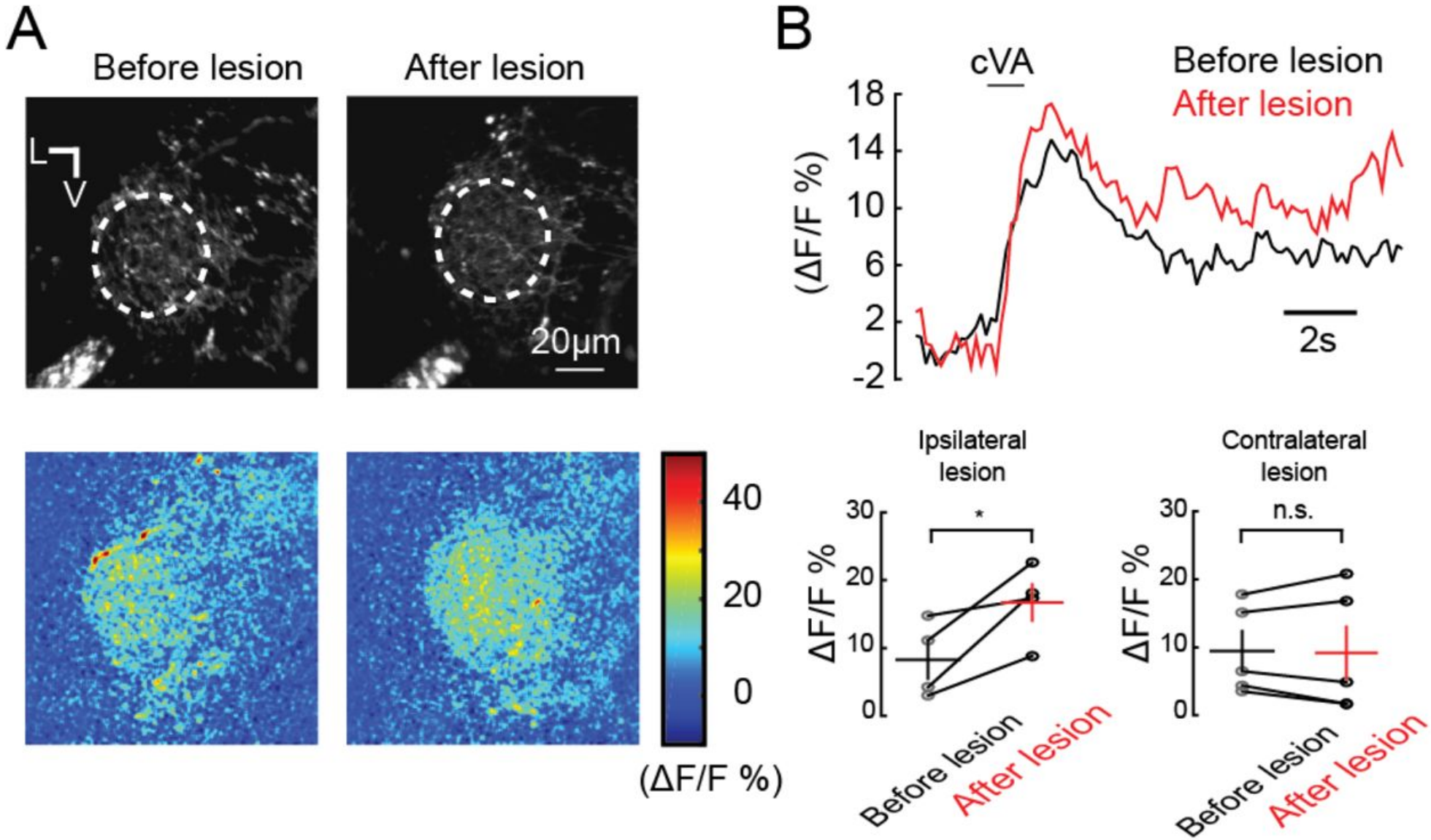
Figure 4 figure supplement 2